Techniques developed for high-speed AFM

doi: 10.1007/978-3-642-22173-6_1

Techniques developed for high-speed AFM

Toshio Ando

Department of Physics, Kanazawa University, Kakuma-machi, Kanazawa 920-1192, Japan

Abstract This article describes fundamental devices and control techniques that have materialized high-speed atomic force microscopy (AFM) capable of recording dynamic processes of individual biomolecules on video at an imaging rate of 10-25 frames/s, without disturbing their biological functions.

Introduction

There is no doubt that new research fields will be pioneered if we can attain a tool that allows directly observing nanometer-scale dynamic phenomena occurring in liquids or at the solid-liquid interfaces. Not only biomolecular phenomena of course, a vast array of reactions occur under liquid environments, including electro-chemical reaction, corrosion, cleaning by detergent, non-biological catalytic reactions, and so on. Among available microscopy techniques, AFM has almost all capabilities that make such observations possible but lacks one capability, *i.e.*, high temporal resolution.

The low imaging rate of AFM arises from its fundamental operation mechanism, *i.e.*, mechanical scanning and mechanical sensing. The relative horizontal position between a cantilever tip and a sample is changed by raster scanning of either of a cantilever tip or the sample stage. A local portion of the sample surface is sensed by a cantilever tip interacting with the surface, and this interaction is transmitted to the cantilever, resulting in the deflection of the cantilever beam. When the cantilever is oscillated in the z-direction, the tip-sample interaction results in a change

in the oscillation amplitude, phase, or resonant frequency. One of these mechanical signals is maintained constant during the xy-scanning by moving the scanner in the z-direction under feedback control. As a result, the movement of the scanner approximately traces the sample surface. Therefore, the sample height map over the xy-scan area is reconstructed from the signals driving the scanner in the z-direction at respective xy positions.

To increase the imaging rate of AFM, we first need to increase the speed of the mechanical scanning and sensing without generating unwanted vibrations. For biological applications, we further need to minimize the tip-sample interaction force, without deteriorating the imaging speed. In the past 20 years, many efforts have been carried out to materialize high-speed AFM. However, only a few groups have been participated in developing the entire system of high-AFM [1-4]. In this article, I focus on the technical development carried out in my group, and show a few results of high-speed AFM imaging of bacteriorhodopsin. For a historical view of the last 20 years in this field, see reviews [5-7].

Imaging speed and feedback bandwidth

In bio-AFM imaging, it is mandatory to maintain the tip-sample distance (hence, tip-sample interaction force) constant under feedback control. When a sample is scanned over an area of $W \times W$ with scan velocity V_s in the x-direction and N scan lines in the y-direction, the image acquisition time T is given by $T = 2WN/V_s$. Supposing that the sample surface is characterized with a single spatial frequency $1/\lambda$, then the feedback scan is executed in the z-direction with frequency $f = V_s/\lambda$ to trace the sample surface. The feedback bandwidth f_B of the microscope should be equal to or higher than f, and thus, we obtain the relationship $T \geq 2WN/(\lambda f_B)$.

The feedback bandwidth is usually defined by a feedback frequency at which a closed-loop phase delay of $\pi/4$ occurs in tracing the sample surface. The phase delay in the closed loop (φ_{closed}) is approximately twice that in the open loop (φ_{open}), provided the feedback gain is maintained at ~1 [4]. The phase delay is caused by the limited response speed of devices contained in the feedback loop and by the

time delay due to a below-mentioned 'parachuting' effect. By denoting the total time delay by $\Delta\tau_{total}$, φ_{open} is given by $\varphi_{open} = 2\pi f\Delta\tau_{total}$. The phase delay can be compensated by a factor of α (2-3) using the (P + D) operation of the proportional-integral-derivative (PID) feedback controller. f_B is thus given by $f_B = \alpha/(16\Delta\tau_{total})$. Hence, the highest possible imaging rate (V_{max}) is give by $V_{max} = \alpha\lambda/(32WN\Delta\tau_{total})$, when the sample fragility is not taken into account. To materialize, for example, an imaging rate of 25 frames/s for $\alpha = 2.5$, $\lambda = 10$ nm, $W = 200$ nm, and $N = 100$, we have to achieve $f_B > 100$ kHz and thus $\Delta\tau_{total} < 1.6$ μs. The time delays at respective devices and at parachuting are described in the following sections.

Mechanical devices in high-speed AFM

Cantilevers

The response time of a cantilever τ_c is expressed by $\tau_c = Q_c/(\pi f_c)$, where Q_c and f_c are the quality factor and resonant frequency of a cantilever, respectively. To shorten the response time, we need a high f_c and a small Q_c. A high f_c together with a small spring constant k_c can be achieved by reducing the cantilever size [8]. We developed small cantilevers collaborating with Olympus [3, 4]. The most recent small cantilevers made of Si_3N_4 are ~6 μm long, 2 μm wide, and 90 nm thick (Fig. 1a), resulting in f_c in air 3.5 MHz, f_c in water 1.2 MHz, k_c ~0.2 N/m, and Q_c in water 2-3 [9]. Therefore, its response time in water is about 0.66 μs. Somewhat larger cantilevers (BL-AC10DS-A2, Olympus: f_c in air 1.5 MHz, f_c in water 600 kHz, k_c ~0.1 N/m) are already commercially available (Atomic Force F&E

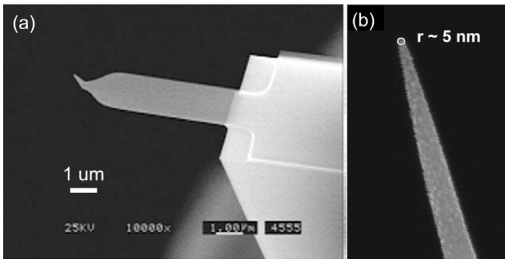

Fig. 1. SEM images of small cantilever (a) and EBD tip (b).

GmbH).

In addition to the advantage in achieving a high imaging rate, small cantilevers have other advantages. The total thermal noise only depends on the spring constant and the temperature. Therefore, a cantilever with a higher resonant frequency has a lower noise density. In addition, shorter cantilevers have higher optical beam deflection (OBD) detection sensitivity, because the sensitivity follows $\Delta\varphi/\Delta z = 3/(2L)$, where Δz is the displacement and $\Delta\varphi$ is the change in the angle of a cantilever free-end. A high resonant frequency and a small spring constant result in a large ratio (f_c/k_c), which gives the cantilever high sensitivity to the gradient (k) of the force exerted between the tip and the sample, because the gradient of the force shifts the cantilever resonant frequency by approximately $-0.5kf_c/k_c$. Therefore, small cantilevers with large values of f_c/k_c are useful for phase-contrast imaging and frequency-modulation AFM (FM-AFM).

The tip apex radius of the small cantilevers developed by Olympus is ~17 nm, which is not sufficiently small for the high-resolution imaging of biological samples. We usually attach a sharp tip on the original tip by electron-beam deposition (EBD) in phenol gas [4]. A piece of phenol crystal (sublimate) is placed in a small container with small holes (~0.1 mm diameter) in the lid. The container is placed in a scanning electron microscope (SEM) chamber under a low-vacuum condition, and cantilevers are placed immediately above the holes. A spot-mode electron beam is irradiated onto the cantilever tip, which produces a needle on the original tip at a growth rate of ~1 μm/min. The newly formed tip has an apex radius of ~25 nm and is sharpened by plasma etching in argon or oxygen gas (Fig. 1b), which decreases an apex radius to ~4 nm in the best case. The mechanical durability of this sharp tip is not high but is still sufficient to be used to capture many images.

Scanner

Tube scanners that have been often used for conventional AFM are inadequate for high-speed AFM, as their long and thin structure lowers the resonant frequencies in the x-, y-, and z-directions. The structural resonant frequency can be enhanced

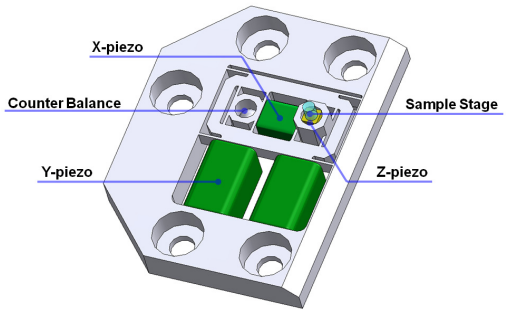

Fig. 2. Structure of high-speed scanner.

by adopting a compact structure. However, a compact structure tends to produce interference (crosstalk) between the three scan axes. To minimize the crosstalk, we employ flexures (blade springs) that are sufficiently flexible to be displaced but sufficiently rigid in the directions perpendicular to the displacement axis (Fig. 2). In our scanner, the y-scanner moves the x-scanner, the x-scanner moves the z-scanner, and the z-scanner moves a sample stage [10]. In the most recent x-scanner, a piezoactuator is inserted between two identical flexures so that the center of mass is unchanged while the piezoactuator is displaced (Fig. 2) [4]. One of the flexure is connected with the z-scanner while the other is connected with an identical dummy z-scanner for counter balancing. The whole scanner framework is made by monolithically processing a single metal block to minimize the number of resonant elements. The lowest resonant frequency of the x-scanner is ~60 kHz. The maximum displacements of the x- and y-scanners are ~2 μm.

The response time of the z-scanner (τ_z) is expressed by $\tau_z = Q_z/(\pi f_z)$, where Q_z and f_z are the quality factor and resonant frequency of the z-scanner, respectively. f_z is almost solely determined by the resonant frequency of a piezoactuator used and by how to hold the piezoactuator to completely suppress the structural resonance arising from the surrounding framework. In the most recent z-scanner, a piezoactuator with a resonant frequency of ~450 kHz is held at the four rims parallel to the displacement direction (Fig. 2) [11]. In this way of holding, the center of mass of the

piezoactuator is not displaced (hence, no impulsive force is exerted on the supporting mechanism), and importantly, the resonant frequency of the z-piezoactuator is nearly unchanged. The maximum displacement is ~1 μm.

Active damping techniques

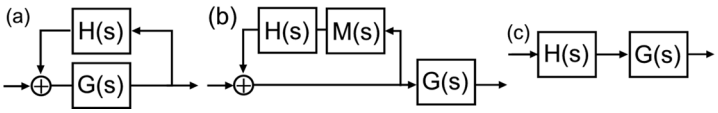

Fig. 3. Diagrams of feedback and feedforward active damping for scanner vibrations. (a) conventional feedback Q-control, (b) feedback Q-control with mock scanner, (c) feedforward control. G(s), H(s), and M(s) represent a resonant system to control, an operator for control, and a mock resonant system, respectively.

Feedback Q-control for z-scanner

In the diagram shown in Fig. 3a, the operator $H(s)$ converts the resonant system $G(s)$ to a target system $R(s)$ expressed as

$$R(s) = G(s)/[1 - G(s)H(s)]. \tag{1}$$

Here, let us consider the simplest case where $G(s)$ consists of a single resonant element with resonant frequency ω_1 and quality factor Q_1. The target system is expressed as a single resonator with resonant frequency ω_0 and quality factor Q_0 ($< Q_1$). For these systems, $H(s)$ is expressed as

$$H(s) = \frac{1}{G(s)} - \frac{1}{R(s)} = \left(\frac{s^2}{{\omega_1}^2} + \frac{s}{Q_1\omega_1} + 1\right) - \left(\frac{s^2}{{\omega_0}^2} + \frac{s}{Q_0\omega_0} + 1\right). \tag{2}$$

To eliminate the second-order term from $H(s)$, ω_0 should equal ω_1, which results in

$$H(s) = -\left(\frac{1}{Q_0} - \frac{1}{Q_1}\right)\frac{s}{\omega_1} \quad . \tag{3}$$

This $H(s)$ is identical to a derivative operator with gain = −1 at the frequency $\hat{\omega}$ = $Q_0Q_1\omega_1/(Q_1 - Q_0)$. By adjusting the gain parameter of the derivative operator, we can arbitrarily change the target quality factor Q_0. This method is known as 'Q-control'. When this method is applied to z-scanner, we must measure the displacement (*i.e.*, the output of $G(s)$) or velocity of the z-scanner. However, it is difficult to do so. This problem is solved by using a mock z-scanner $M(s)$ (a second-order low-pass filter) characterized by a transfer function similar to that of the lowest resonant component of the real z-scanner (Fig. 3b) [12].

Since the real z-scanner usually has additional higher resonant components, this simple Q-control is not satisfactory. When elemental resonators are connected in series, we can use mock scanners, $M_1(s)$, $M_2(s)$, - - -, each of which is characterized by a transfer function representing each elemental resonator. Each mock scanner is controlled by a corresponding Q-controller. For example, when the scanner consists of two resonators connected in series, the composite transfer function $C(s)$ of the total system is expressed as

$$C(s) = \frac{1}{1 - M_1(s)H_1(s)} \times \frac{1}{1 - M_2(s)H_2(s)} \times G_1(s)\,G_2(s) \quad . \tag{4}$$

Since $M_1(s)$ and $M_2(s)$ are the same as (or similar to) $G_1(s)$ and $G_2(s)$, respectively, eq. (4) represents a target system consisting of damped resonators connected in series. Note that we can use $M_1(s)$ and $M_2(s)$ separately, unlike $G_1(s)$ and $G_2(s)$.

When the scanner consists of elemental resonators connected in parallel, active damping becomes more difficult. In this case, we use a mock z-scanner comprised of two low-pass filters connected in parallel, which correspond to the first and second resonant components of the z-scanner. It can not damp the second resonant component significantly but better than the case of using a single low-pass filter [12].

Feedfoward damping of x-scanner

The feedforward control type of active damping (Fig. 3c) is based on inverse compensation (*i.e.*, H(s) ~ 1/G(s)). Generally, inverse compensation-based damping has an advantage in that we can extend the scanner bandwidth. This damping method is much easier to apply to the x-scanner than to the z-scanner, because for the former, the scan waves are known beforehand and are periodic (hence, the frequencies used are discrete; *i.e.*, integral multiples of the fundamental frequency). The waveforms of the x-scan are isosceles triangles characterized by amplitude X_0 and fundamental angular frequency ω_0. Their Fourier transform is given by

$$F(\omega) = 2\pi X_0 \left[\frac{1}{2}\delta(\omega) - \frac{2}{\pi^2} \sum_{k=-\infty}^{+\infty} \frac{1}{k^2}\delta(\omega - k\omega_0) \right] \quad (k : odd) \tag{5}$$

To move the x-scanner in the isosceles triangle waveforms, the input signal $X(t)$ sent to the x-scanner characterized by the transfer function $G(s)$ is given by the inverse Fourier transform of $F(\omega)/G(i\omega)$, which is expressed as

$$X(t) = \frac{X_0}{2} - \frac{4X_0}{\pi^2} \sum_{k=1}^{+\infty} \frac{1}{k^2} \frac{1}{G(ik\omega_0)} cos(k\omega_0 t) \quad (k : odd) \tag{6}$$

In practice, the sum of the first ~10 terms in the series of eq. (6) is sufficient. We can calculate eq. (6) in advance to obtain numerical values of $X(t)$ and output them in succession from a computer through a D/A converter. This method is convenient and works well [4]. However, applying this method to the y-scanner is not practical because the period of 'y-return' (scanning towards the origin after acquiring a frame) is much shorter than the total period of the y-scan (*i.e.*, image acquisition time), and hence, we have to use too many terms in the series expansion of the y-scan waveform. We can simply use a round waveform for the y-return. Rounding the vertexes of the triangle waveforms is also useful for the x-scanner, although the deviation of the scan trajectory from the triangle waveform becomes large.

Practice of active damping of scanner vibrations

Here, we describe the practice of active damping applied to the scanner mentioned above. The z-piezoelectric actuator has a resonant frequency of ~450 kHz under free oscillation. The gain and phase spectra of the mechanical response of the z-scanner are shown with the lines marked with (a) in Fig. 4. The z-scanner exhibited large resonant peaks at 440 kHz and 550 kHz. The resonant frequency of 440 kHz is similar to that of the free oscillation of the piezoelectric actuator. Judging from the phase spectrum, the two resonators are connected in series. We used two mock z-scanners connected in series. The resulting gain and phase spectra are shown with lines marked with (b) in Fig. 4. The peak at 440 kHz was almost completely removed and the frequency that gave a 90° phase delay reached 250 kHz [4]. We could reduce the gain at 440 kHz but did to do so to minimize the phase delay. Since the imaging frequency (*i.e.*, feedback frequency) does not go beyond ~150 kHz, the resonator of 440 kHz with a gain slightly larger than 1 is not excited during imaging.

Next, we show the effect of feedforward type of damping applied to the x-scanner contained in the most recent scanner mentioned above. The x-scanner has a major

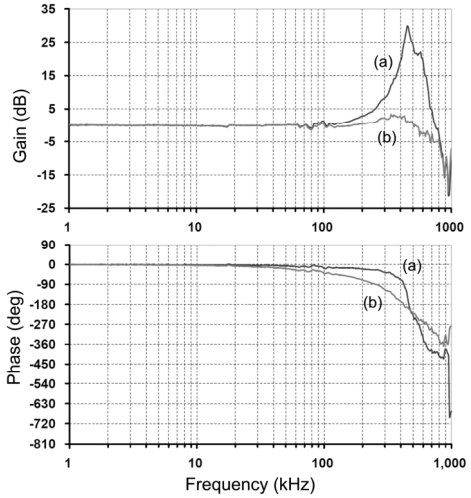

Fig. 4. Frequency response of z-scanner and effect on the response of active damping by feedback Q-control with mock z-scanner. (a) without damping, (b) with damping.

resonance at ~60 kHz and a relatively clean resonant pattern. When the line scan was performed at 3.3 kHz without damping, its displacement exhibited vibrations (Fig. 5a). When it was driven in a waveform calculated using eq. (6) with the maximum term $k = 17$ in the series, the x-scanner moved approximately in a triangle waveform (Fig. 5b) [4]. This damping method also works effectively even for an x-scanner having multiple resonant peaks (Fig. 6a). The maximum displacement of this x-scanner is ~5 μm. When the line scan was performed at 633 Hz with the displacement up to 4 μm, its trajectory showed significant vibrations (Fig. 6b). When feedforward damping was applied, the vibrations were greatly reduced (Fig.6c).

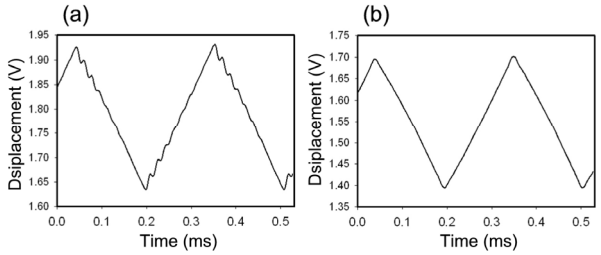

Fig. 5. Displacement of x-scanner and effect of active damping by feedforward control. (a) without damping, (b) with damping.

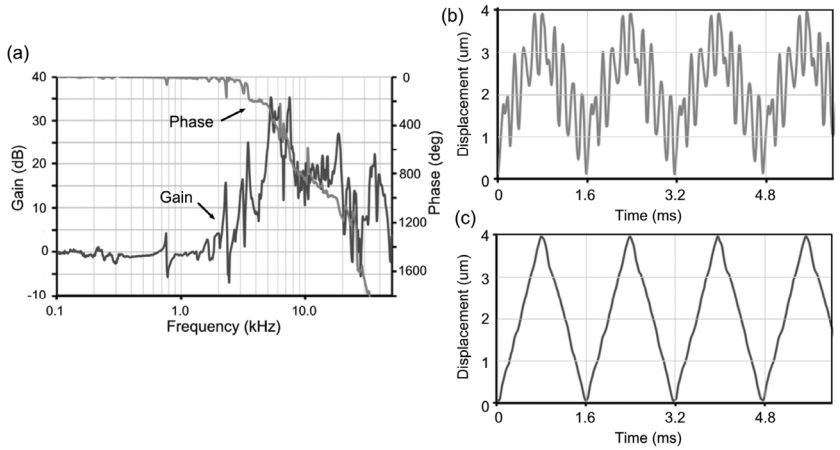

Fig. 6. Frequency response and displacement of wide-range x-scanner and effect of active damping by feedforward control. (a) Frequency response, (b) displacement when feedforward control is not applied, (c) displacement when feedforward control is applied.

Dynamic PID control

In AFM, 'parachuting' means that a cantilever tip completely detaches from a sample surface at a steep down-hill region of the sample and does not re-land on the surface for a while. Parachuting more frequently occurs when the peak-to-peak amplitude set point (A_s) is set closer to the cantilever peak-to-peak free oscillation amplitude ($2A_0$). The error signal is saturated at ($A_s - 2A_0$) during parachuting and the parachuting period is more prolonged when the saturated error signal is smaller. In fact, feedback bandwidth decreases with increasing set point due to parachuting (solid line, Fig. 7). However, for fragile biological samples, the tapping force exerting from an oscillating cantilever tip on the sample has to be minimized by using A_s very close to $2A_0$. To overcome this difficulty, we developed a dynamic PID controller in which the gain parameters are automatically and dynamically changed depending on the cantilever peak-to-peak oscillation amplitude (A) [13].

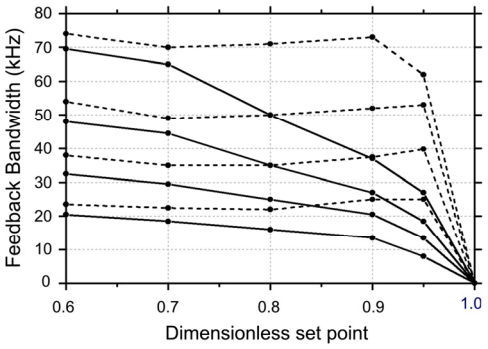

Fig. 7. Feedback bandwidth as a function of set point and effect of dynamic PID control. Dimensionless set point represents the cantilever's peak-to-peak amplitude set point normalized by the peak-to-peak free oscillation amplitude. Solid line, with conventional PID control; Broken line, with dynamic PID control.

The sign of ($A - A_s$) is a good indicator of whether the sample is being scanned at the down-hill region or up-hill region; the plus and minus signs approximately correspond to down-hill and up-hill regions, respectively (note that A cannot be maintained exactly at A_s because of the delay of feedback control). In the dynamic PID controller, the gain parameters are increased when A exceeds A_s (or a level A_t

slightly higher than A_s). The gain increment can be constant or proportional to ($A - A_s$) or ($A_t - A_s$). The dynamic PID controller is effective and the feedback bandwidth becomes independent of A_s as far as A_s is smaller than ~$0.95 \times 2A_0$, indicating that no parachuting occurs under the condition of $A_s < 0.95 \times 2A_0$ (broken line, Fig. 7).

Drift compensator

Using the dynamic PID controller, we can now use a set point A_s very close to the peak-to-peak free oscillation amplitude of a cantilever $2A_0$, without causing parachuting. However, the difference between them ($2A_0 - A_s$) becomes very small when we use a small $2A_0$ for imaging biological samples. Not to disturb the function of biomolecules, we usually have to use $2A_0 \sim$ 2-3 nm, so that the difference ($2A_0 - A_s$) becomes 0.2-0.3 nm under the condition of $A_s = 0.9 \times 2A_0$. This means that even a very small drift in A_0 affects imaging. A cantilever is usually excited by oscillation of a piezoactuator. The temperature of the piezoactuator is elevated during long running, leading to its smaller oscillation and hence to a smaller A_0. Supposing that A_0 decreases by drift and consequently A decreases, the AFM instrument misinterprets this decrease in A as caused by stronger tip-sample interaction than expected. Therefore, the sample stage is withdrawn from the cantilever tip by feedback control, and eventually, the cantilever tip will be completely detached from the sample surface, resulting in inability of imaging. Thus, we need to precisely maintain the free oscillation amplitude constant but there is no way to detect change in the free oscillation amplitude during imaging.

This problem was previously challenged by Schiener *et al* [14]. They monitored the second-harmonic amplitude of the cantilever to detect the drift in A_0. The second-harmonic amplitude is sensitive to the tip-sample interaction, and therefore, the drift in A_0 is reflected in the second-harmonic amplitude averaged over a period longer than the image acquisition time. To compensate for drift in the cantilever excitation efficiency, we controlled the output gain of a wave generator connected to the excitation piezoactuator by measuring and averaging the second-

harmonic amplitude [13]. By this compensation, the cantilever free oscillation amplitude is maintained constant and thus very stable imaging is possible for a long time even with a small difference $(2A_0 - A_s) \sim 0.2$ nm.

Bio-imaging

To demonstrate the high capability of our current high-speed AFM instrument, we here describe some imaging studies carried out on 2D crystals of bacteriorhodopsin, without getting into the biological significance.

Dynamic equilibrium at the bacterirhodopsin crystal edge

The purple membrane (PM) exists in the plasma membrane of *Halobacterium halobium* and its constituent protein, bacteriorhodopsin (bR), functions as a light-driven proton pump. In the PM, bR monomers are associated to form a trimeric oligomer and the trimers are arranged in a hexagonal lattice [15]. In the 2D crystal of bR and any crystals in general, they are in dynamic equilibrium with the constituents at the interface between the crystal and the liquid phase. We visualized dynamic events at the interface in the PM [16].

The PM was adsorbed on a mica surface in a buffer solution (10mM Tris-HCl (pH

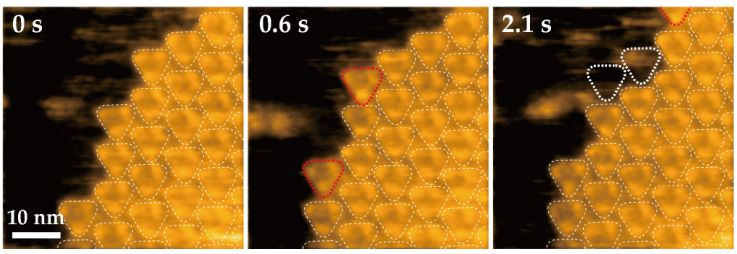

Fig. 8. Time-lapse high-magnification AFM images of PM at the interface between crystalline and non-crystalline area captured at 3 frames/s. The thinlined triangles show bR trimers. The bR trimers encircled by the red dotted line at 0.6 s indicate newly bound bR trimer. The white dotted triangles at 2.1 s indicate the previously bound trimers.

8.0) and 300 mM KCl). Fig. 8 shows typical AFM images taken at 3 frames/s. The bR trimers in the crystal are indicated by the thinlined triangles. At 0.6 s, two bR trimers (red triangles) have newly bound to the crystal edge. Subsequently, two bR trimers (white triangles) have dissociated and another trimer (red triangle) has bound to the crystal edge at 2.1 s. One of the two dissociated trimers remains in the crystal area for ~0.9 s. In order to estimate the inter-trimer interaction energy, we analyzed the residence time of newly bound bR trimers at the crystal edge and its dependence on the number of interaction sites. For the analysis, we assumed that, within the 2D bR crystal, a trimer can interact with the surrounding trimers through six sites. Following this assumption, the number of interaction sites at the crystal edge is reduced, depending on the binding position. Successive AFM images as exemplified in Fig. 8 showed many binding and dissociation events in which bR trimers bound to different sites at the border between the crystal and non-crystal areas. These events can be classified into types 'I', 'II', and 'III' depending on the number of interaction sites involved (Roman numerals indicate the number of interaction bonds). Type II binding events are predominant (~74%), whereas type I (~6 %) and type III (~20%) bindings are minor events. The lifetime of the type I bonds was too short to obtain clear images of the corresponding event, preventing reliable statistics.

Fig. 9a shows a histogram of the lifetime for type II bond which was measured using AFM images taken at 10 frames/s. The histogram can be well fitted by a single exponential (correlation coefficient, r = 0.9), from which the average lifetime τ_2

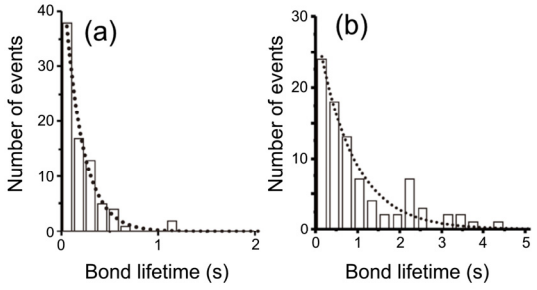

Fig. 9. (a) Histogram showing the lifetime distribution of type *II* binding events. The histogram was fitted by a single-exponential function (dotted line). (b) Histogram showing the lifetime distribution of type *III* binding events. The histogram was fitted by a single-exponential function (dotted line).

was estimated to be 0.19 ± 0.01 s. Fig. 9b shows a histogram of the type III bond lifetime, from which the average lifetime τ_3 was estimated to be 0.85 ± 0.08 s. The longer lifetime of type III bonds compared with type II obviously arises from a relationship of $E_{III} < E_{II} < 0$, where E_{II} and E_{III} are the association energies responsible for type II and type III interactions, respectively. The average lifetime ratio, τ_2/τ_3, is given by

$$\tau_2 / \tau_3 = exp[-(E_{III} - E_{II})/(k_B T)]. \quad (7)$$

Because the type II interaction contains two elementary bonds, whereas the type III interaction contains three, the energy difference $E_{III} - E_{II}$ corresponds to the association energy of the single elementary bond. From the ratio $\tau_2/\tau_3 = 0.22$ and Eq. (7), this elementary association energy is estimated to be about $-1.5\ k_B T$, which corresponds to –0.9 kcal/mol at 300 K [16]. This value is approximately consistent with that estimated by differential scanning calorimetry [17, 18].

The association energy of the type II bond is only $-3.0\ k_B T$. Nevertheless, the residence time for the type II bond was independent of the scan speed (60-105 μm/s corresponding to the imaging rate 8-14 frames/s). This is a clear indication that very weak tip-sample interaction is achieved even at such high imaging rates.

Structural changes of bacteriorhodopsin under light

Since bR is a light-driven proton pump, the detection of its structural change upon absorption of light has long been a goal. bR contains seven transmembrane α-helices (named A–G) enclosing the chromophore retinal [19, 20]. Absorption of light by the retinal triggers a cyclic reaction (photocycle) that comprises a series of spectroscopically identified intermediates, designated as the J, K, L, M, N, and O states [21]. The light-induced conformational changes in bR have been investigated by various methods [22-26], leading to a consensus that the proton channel at the cytoplasmic surface is opened by the tilting of helix F away from the protein center [25, 26]. This movement of helix F leads to a rearrangement of the E-F

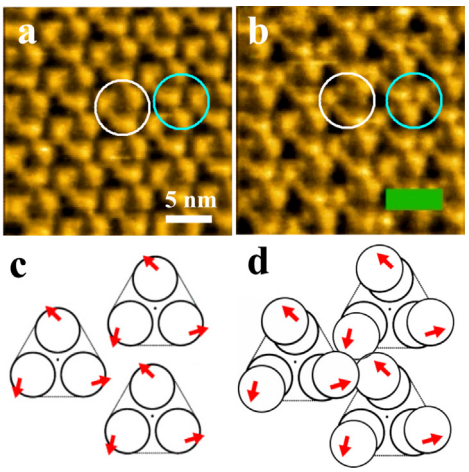

Fig. 10. High-speed AFM images of the cytoplasmic surface of D96N under dark (a) or illuminated (b) conditions. The green bar indicates light illumination. A trimer is highlighted by the white circles and a trefoil is highlighted by the light-blue circles. The direction of the conformational change in bR is shown by the red arrows (c, d). By the outward movement, bR monomers in a trefoil are brought into contact with each other (d).

loop, which results in large-scale conformation changes in the M and N intermediates. Recently, we directly captured the photo-induced conformational change at cytoplasmic surface of bR using high-speed AFM [27].

The photocycle of wild-type bR completes in ~10 ms at pH 7.0 and therefore the photo-activated intermediate states are too brief to be clearly captured by high-speed AFM. Thus, we used the D96N mutant that has a longer photocycle (~10 s) at pH 7.0 but retains an ability of proton pumping. Fig. 10a and b show successive images of D96N at the cytoplasmic surface captured at 1 frame/s. Under the unphotolyzed state (Fig. 10a), one can clearly see individual bR molecules forming well-ordered trimers in the two-dimensional hexagonal lattice. A trimer is encircled by the white circle. Upon illumination with green light, bR drastically changes its structure as shown in Fig. 10b. This activated state with a unique structure returns to the prior unexcited state in a few seconds after light-off. This cyclic structural change is highly reproducible in repeated dark-illumination cycles. On the other hand, significant conformational changes of bR are not observed on the extracellular surface.

We analyzed the center of mass for each monomer during the dark-illumination cycles. Each activated bR monomer displaced outward from the center of trime by ~0.7 nm on average (the direction of the movement is shown by arrows in Fig. 10c). As a result, three nearest-neighbor bR monomers, each of which belongs to a different adjacent trimer, are brought into contact with each other (Fig. 10d). Here, we use a new designation, 'trefoil', for the triad of the nearest-neighbor monomers (shown by the light-blue circles in Fig. 10a and b) to distinguish it from the original trimer. Remarkably, this transient assembly in a trefoil alters the decay kinetics of the activated state [27].

As demonstrated above, direct and dynamic observation of functioning protein molecules is a powerful new approach to studying conformational changes in proteins induced by external stimuli.

Conclusion

We believe that the techniques for increasing the imaging speed of AFM have already been almost matured. Further increasing the speed would be very difficult unless completely different approaches are introduced, such as self-sensing and self-actuation small cantilevers with a small spring constant. We have mostly employed analogue circuits to construct the high-speed AFM instrument. The analogue system lacks flexibility. For example, the analogue feedback Q-controller has to be newly constructed whenever a new scanner is developed. At present, digital systems such as FPGA and DSP are not fast enough. FPAA (Field Programmable Analogue Array), an analogue system corresponding to FPGA, is now becoming available (*e.g.*, Anadigm) but the bandwidth of analogue components used therein is not yet high enough. However, this situation will change in the near future and high-speed AFM systems with high flexibility and adaptability will be able to be constructed.

Recent studies of high-speed AFM imaging of proteins have demonstrated the usefulness of this new microscopy in biology [26-30]. Previously known and unknown behaviors of proteins clearly appear in the molecular movies simultaneous-

ly. Even for known behaviors, the high-resolution movies provide corroborative 'visual evidence'. Unlike previous methods, high-resolution AFM imaging unselectively provides the comprehensive information on the structure and dynamics of a functioning molecule. Thus, the high-speed AFM imaging of functioning biomolecules has the potential to transform the field of structural biology. In addition, high-speed AFM will provide a new approach to studying nanometer-scale dynamic phenomena occurring in liquids and at the solid-liquid interfaces, and therefore, will greatly contribute to creating new nanotechnology.

References

1. Viani, M. B., Richter, M., Rief, M., Gaub, H. E., Plaxco, K. W., Cleland, A. N., Hansma, H. G. & Hansma, P. K. Fast imaging and fast force spectroscopy of single biopolymers with a new atomic force microscope designed for small cantilevers. *Rev. Sci. Instrum*. **70**, 4300-4303 (1999).
2. Fantner, G. E. Schitter, G., Kindt, J. H., Ivanov, T., Ivanova, K., Patel, R., Holten-Andrersen, N., Adams, J., Thurnera, P. J., Rangelowb, I. W. & Hansma, P. K. Components for high-speed atomic force microscopy. *Ultramicroscopy* **106**, 881-887 (2006).
3. Ando, T., Kodera, N., Takai, E., Maruyama, D., Saito, K. & Toda, A. High-speed atomic force microscope for studying biological macromolecules. *Proc. Natl. Acad. Sci. USA* **98**, 12468-12472 (2001).
4. Ando, T., Uchihashi, T. & Fukuma, T. High-speed atomic force microscopy for nano-visualization of dynamic biomolecular processes. P*rog. Surf. Sci.* **83,** 337-437 (2008).
5. Ando, T., Uchihashi, T., Kodera, N., Yamamoto, D., Taniguchi, M., Miyagi, A. & Yamashita, H. Review: High-speed atomic force microscopy for observing dynamic biomolecular processes. *J. Mol. Recognit*. **20**, 448-458 (2007).
6. Ando, T., Uchihashi, T., Kodera, N., Yamamoto, D., Taniguchi, M., Miyagi, A. & Yamashita, H. Invited Review: High-speed AFM and nano-visualization of biomolecular processes. *Pflüuger Archiv – Eur. J. Physiol*. **456**, 211-225 (2008).
7. Hansma, P. K., Schitter, G., Fantner, G. F. & Prater, C. High-speed atomic force microscopy. *Science* **314**, 601-602 (2006).
8. Walters, D. A., Cleveland, J. P., Thomson, N. H., Hansma, P. K., Wendman, M. A., Gurley, G. & Elings, V. Short cantilevers for atomic force microscopy. *Rev. Sci. Instrum*. **67**, 3583-3590 (1996).
9. Kitazawa, M., Shiotani, K. & Toda, A. Batch fabrication of sharpened silicon nitride tips. *Jpn. J. Appl. Phys*. **42**, 4844-4847 (2003).
10. Ando, T., Uchihashi, T., Kodera, N., Miyagi, A., Nakakita, R., Yamashita, H. & Matada, K. High-speed AFM for studying the dynamic behavior of proteins molecules at work. *Surf. Sci. Nanotechnol*. **3**, 384-392 (2005).
11. Fukuma, T., Okazaki, Y., Kodera, N., Uchihashi, T. & Ando, T. High resonance frequency force microscope scanner using inertia balance support. *Appl. Phys. Lett*. **92**, 243119 (2008).
12. Kodera, N., Yamashita, H. & Ando, T. Active damping of the scanner for high-speed atomic force microscopy. *Rev. Sci. Instrum.* **76**, 053708 (5 pp.) (205).
13. Kodera, N., Sakashita, M. & Ando, T. Dynamic proportional-integral-differential controller for high-speed atomic force microscopy. *Rev. sci. Instrum*. **77**, 083704 (7 pp.) (2006).

14. Schiener, J., Witt, S., Stark, M. & Guckenberger, R. Stabilized atomic force microscopy imaging in liquids using second harmonic of cantilever motion for set-point control. *Rev. Sci. Instrum*. **75**, 2564-2568 (2004).
15. Henderson, R., Baldwin, J. M., Ceska, T. A., Zemlin, F., Beckmann, E. and Downing, K. H. Model for the structure of bacteriorhodopsin based on high-resolution electron cryo-microscopy, *J. Mol. Biol.,* **213**, 899-929 (1990).
16. Yamashita, H. Voïtchovsky, K., Uchihashi, T. Contera, S. A., Ryan, J. F. and Ando, T. Dynamics of bacteriorhodopsin 2D crystal observed by high-speed atomic force microscopy, *J. Struc. Biol.*, **167**, 153-158 (2009).
17. Jackson, M. B. and Sturtevant, J. M. Phase transitions of the purple membranes of Halobacterium halobium, *Biochemistry,* **17**, 911-915 (1978).
18. Koltover, I., Raedler, J.O., Salditt, T., Rothschild, K.J. and Safinya, C.R. Phase behavior and interactions of the membrane-protein bacteriorhodopsin, *Phys. Rev. Lett.*, **82**, 3184-3187 (1999).
19. Kimura, Y., Vassylyev D. G., Miyazawa A., Kidera A., Matsushima M., Mitsuoka K., Murata K., Hirai T. and Fujiyoshi Y. Surface of bacteriorhodopsin revealed by high-resolution electron crystallography. *Nature*, **389**, 206-211 (1997).
20. Luecke, H., Schobert, B., Richter, H.T., Cartailler, J.P. and Lanyi, J.K. Structure of bacteriorhodopsin at 1.55 Å resolution. *J. Mol. Biol.*, **291**, 899-911 (1999).
21. Lanyi, J.K. Bacteriorhodopsin. *Annu. Rev. Physiol.* **66**, 665-688 (2004).
22. Dencher, N.A., Dresselhaus, D., Zaccai, G. and Büldt, G. Structural changes in bacteriorhodopsin during proton translocation revealed by neutron diffraction. *Proc. Natl. Acad. Sci. USA* **86**, 7876-7879 (1989).
23. Subramaniam, S., Gerstein, M., Oesterhelt, D. and Henderson, R. Electron diffraction analysis of structural changes in the photocycle of bacteriorhodopsin. *EMBO J.*, **12**, 1-8 (1993).
24. Brown, L.S., Needleman, R. and Lanyi, J.K. Conformational change of the E-F interhelical loop in the M photointermediate of bacteriorhodopsin. *J. Mol. Biol.* **317**, 471-478 (2002).
25. Sass, H.J., Büld G., Gessenich R., Hehn D., Neff D., Schlesinger R., Berendzen J. and Ormos P. Structural alterations for proton translocation in the M state of wild-type bacteriorhodopsin. *Nature* **406**, 649-653 (2000).
26. Subramaniam, S. & Henderson, R. Molecular mechanism of vectorial proton translocation by bacteriorhodopsin. *Nature* **406**, 653-657 (2000).
27. Shibata M., Yamashita H., Uchihashi T., Kandori H. and Ando T. High-speed atomic force microscopy shows dynamic molecular processes in photo-activated bacteriorhodopsin. *Nature Nanotech*. **5**, 208-212 (2010).
28. Yamamoto, D., Nagura, N., Omote, S., Taniguchi, M. & Ando, T. Streptavidin 2D crystal substrates for visualizing biomolecular processes by atomic force microscopy. *Biophys. J.* **97**, 2358-2367 (2009).
29. Yamamoto, D., Uchihashi, T. Kodera, N. & Ando, T. Anisotropic diffusion of point defects in two-dimensional crystal of streptavidin observed by high-speed atomic force microscopy. *Nanotechnology* **19**, 384009 (9 pp.) (2008).
30. Miyagi, A., Tsunaka, Y., Uchihashi, T., Miyanagi, K. Hirose, S., Morikawa, K. & Ando, T. Visualization of intrinsically disordered regions of proteins by high-speed atomic force microscopy. *Chem. Phys. Chem*. **9**, 1859-1866 (2008).